tauopathies. Interestingly, right-side dominant [^{11}C]PBB3-PET signals in the basal ganglia were consistent with laterality of atrophy in this area (Figure S8F). These findings may also be associated with a right-side dominant decrease in cerebral blood flow and left-side dominant motor signs in this patient.

DISCUSSION

Here, we report our efforts to develop BBB-penetrant ligands that are capable of binding to and visualizing intracellular tau aggregates in AD and non-AD tauopathies. These compounds may accordingly be useful for the differential diagnosis of neurological conditions in elderly subjects on the basis of the distribution of tau lesions, thereby opening up novel avenues for research in elucidating mechanisms of tau-mediated neurodegeneration, as well as tau-focused biomarkers and therapies.

Despite numerous efforts to develop imaging ligands to visualize tau pathologies in the brains of patients with AD and related tauopathies, the urgent need for these tau biomarkers remains largely unmet. To address this significant challenge, we also took advantage of a multimodal imaging system, which facilitates a quick and label-free validation of candidate compounds in terms of their transfer to the brain and retention in tau-rich regions. In addition, subcellular-resolution imaging optics exemplified by two-photon laser scanning microscopy provided proof of the rapid transfer of intravenously administered potential tau pathology imaging agents from plasma to the CNS extracellular matrix and subsequently to the cytoplasm of neurons, where they can bind to intracellular tau inclusions. Based on these encouraging preliminary data using nonlabeled compounds, a subset of these compounds was radiolabeled for use in PET imaging of Tg mice that model tau pathology, and a radioligand that yielded the best visualization of tau lesions in these Tg mice was selected for further testing in human AD patients and NC subjects as well as patients with probable CBD. This stepwise strategy enabled us to identify and advance the most promising PET probe for the visualization and quantitative assessment of tau pathology in the CNS of living human subjects. Interestingly, another research group has recently reported development of ^{18}F-labeled PET ligands for tau lesions mostly through assessments of binding to brain tissues, but not recombinant tau assemblies (Zhang et al., 2012; Chien et al., 2013), as in the present approach. These radioligands have been implied to produce considerably high contrasts for tau pathologies in living AD brains, and relatively long radioactive half-life of ^{18}F would enable delivery of radioligands from a radiosynthesis sites to multiple PET facilities. [^{11}C]PBB3 has distinct advantages over these compounds, as exemplified by affinity for diverse tau lesions, including Tg mouse tau aggregates, applicability to multimodal imaging, and induction of smaller radioactive exposure than ^{18}F-labeled ligands.

In the present work, we clinically validated the performance of [^{11}C]PBB3 as a tau imaging agent by comparing the distribution of [^{11}C]PBB3 with that of [^{11}C]PIB in AD brains. Tau deposits in patients with moderate or severe AD are thought to be distributed extensively in the neocortical and limbic regions (classified as Braak stage V/VI) (Braak and Braak, 1991), thereby resembling localization of senile plaques, except for the predominance of tau aggregates in the hippocampal formation. This rationalizes the use of radioactivity in the medial temporal area as an index to validate an imaging probe for tau pathology versus Aβ deposits in AD patients from prodromal to advanced stages. Furthermore, our preliminary data suggest that [^{11}C]PBB3 may be capable of capturing the temporospatial spreading of neurofibrillary tau pathologies from the limbic system (Braak stage III/IV or earlier) to neocortical areas (Braak stage V/VI) with the progression of AD (Figure 8). A considerable subset of tau lesions at Braak stage I/II is composed of phosphorylated tau deposits barely reactive with thioflavin-S (i.e., pretangles), and NFTs are relatively low in number and are confined to the transentorhinal cortex (Braak and Braak, 1991; Braak et al., 2011). Therefore, detection of these early tau pathologies would be more difficult. Our next-stage clinical study with expanded sample size and wider range of MMSE scores is currently ongoing to pursue tau accumulation in normal controls and subjects with mild cognitive impairments and AD at diverse stages and will bring more compelling insights into the significance of tau PET imaging in early diagnosis and prediction of AD. In addition, alterations of [^{11}C]PBB3 retention were indicated in the transition from mild to moderate AD. Loss of PET signals in the lateral temporal cortex of a patient with moderate AD (subject 6 in Figure 8) might not result from atrophy of this region, as the hippocampus of the same subject exhibited strong [^{11}C]PBB3 binding despite marked atrophy. Possible explanations for this change include formation of extracellular NFTs and their envelopment by astrocytes in the degenerating neocortex, profoundly modifying accessibility of these NFTs to exogenous molecules (Schmidt et al., 1988). This notion would need to be examined by combined autoradiogarphic and immunohistochemical assays of different brain regions.

Being able to visualize tau deposits with [^{11}C]PBB3 in non-AD tauopathies, such as PSP, CBD, and related disorders, is also of major importance, as suggested in the present PET data the support detectability of tau deposition in living CBD brains. As compared with NFTs and neuropil threads in AD, abundant tau deposits are largely confined to specific neuroanatomical locations of the CNS in tau-positive, plaque-negative illnesses, as exemplified by PSP and CBD (Dickson et al., 2011), but the homogenous and low-level background signals of [11C]PBB3 in brain parenchyma indicate the possibility of detecting tau lesions in these disorders. Following such in vivo assessments, a postmortem neuropathological evaluation of scanned subjects would be required as a reference standard for PET assays of non-AD tau pathologies.

[^{11}C]PIB-positive plaque formation nearly plateaus prior to the progression of brain atrophy in AD (Engler et al., 2006), but tau abnormalities may bridge the chasm between Aβ fibrillogenesis and neuronal death. Consistent with this notion, our PET/MRI data indicate that the deposition of tau inclusions as visualized by the intense [^{11}C]PBB3 labeling but lacking overt [^{11}C]PIB binding is closely associated with a local volume reduction in the hippocampal formation. Indeed, our pilot clinical PET study demonstrated that localized accumulation of [^{11}C]PBB3 in the medial temporal region of AD patients was accompanied by marked hippocampal atrophy (Figure 7B). Notably, [^{11}C]PBB3-PET signals were substantially increased, notwithstanding the atrophy-related partial volume effects on PET images, and this

observation may support the contribution of tau fibrils to toxic neuronal death in AD. However, these data do not immediately imply neurotoxicities of [^{11}C]PBB3-reactive tau fibrils, in light of MRI-detectable neurodegeneration uncoupled with [^{11}C]PBB3 retention in the hippocampus of PS19 mice. In the hippocampal formation of AD patients, neurons bearing NFTs that resemble those in the PS19 hippocampus may drive neurodegeneration similar to that observed in either the PS19 hippocampus or brain stem, and this issue could be addressed in future studies using [^{11}C]PBB3-PET and MRI in diverse mouse models, including PS19 and rTg4510 mice, and human subjects.

Our analyses of multiple β sheet ligands illustrated electrochemical and/or conformational diversities of β-pleated sheets among amyloid aggregates, producing a selectivity of these compounds for a certain spectrum of fibrillar pathologies (Figures 1 and S1). Lipophilicities of the β sheet ligands could determine their reactivity with noncored plaques, as noted among the PBBs studied here (Figure 1), although the molecular properties underlying this variation are yet to be elucidated. Meanwhile, we noted that all β sheet ligands tested in the present study were reactive with dense core plaques regardless of their lipophilicities. This may affect in vivo PET signals, particularly in AD brain areas with abundant cored plaques, such as the precuneus. However, our combined autoradiographic and histochemical assessments indicated that [^{11}C]PBB3 bound to dense core plaques accounts for less than 10% of total specific radioligand binding in these areas, and this percentage in fact includes binding to tau fibrils in plaque neurites in addition to Aβ amyloid core. A second possibility to account for the diversity of ligand reactivity to tau lesions may arise from the packing distance between two juxtaposed β sheets in tau filaments and is discussed in the Supplemental Discussion.

Notably, selectivity of [^{11}C]PBB3 for tau versus aggregates may depend on free radioligand concentration in the brain. Our autoradiographic binding assays suggested that affinity of [^{11}C]PBB3 for NFTs is 40- to 50-fold higher than senile plaques, but binding components on tau fibrils may be more readily saturated by this radioligand than those on Aβ fibrils. [^{11}C]PBB3-PET data in humans indicated that uptake of this radioligand into the brain is less than one-third of [^{11}C]PIB uptake and that free radioligand concentration in the brain at a pseudoequilibrium state is approximately 0.2 nM or lower. In this range of concentration, [^{11}C]PBB3 could preferentially interact with high-affinity binding components formed by tau assemblies. An excessive amount of radioligand in the brain would result in saturation of radioligand binding to tau lesions and increased binding to low-affinity, high-capacity binding components in Aβ plaques, and such overload of free radioligand is more likely in regions with less abundant tau pathologies. This could be even more critical in capturing early tau pathologies that originate in the hippocampal formation and may require technical improvements and methodological refinements, including high-resolution imaging, correction for motions of subjects during scans, and robust definition of VOIs on the atrophic hippocampus.

Although nonspecific [^{11}C]PBB3-PET signals in control human subjects were generally low, radioligand retention in dural venous sinuses was noticeable in all scanned individuals. Possible mechanisms that underlie this property are discussed in the Supplemental Discussion.

The present work has also implied the potential utility of multimodal imaging systems for translational development of therapeutic agents that counteract tau fibrillogenesis. Optical imaging with a near-infrared fluorescent probe, such as PBB5, could provide the least invasive technique to assess tau accumulation in living mouse models. As demonstrated by our in vitro and ex vivo fluorescence labeling, all PBBs share a similarity in terms of their reactivity with tau aggregates. Hence, PBB5 optics may be applicable to early screening of therapeutic agents that suppress tau deposition, and the data on abundance of tau lesions obtained by this approach may be translatable to advanced stages of assessments using [^{11}C]PBB3-PET in animal models and humans. By contrast, pharmacokinetic properties of PBB5 (Figure S5) were found to be distinct from those of electrically neutral PBBs, including PBB2 and PBB3. These considerations would be of importance in developing and using fluorescent ligands applicable to optical and PET imaging.

To conclude, our class of multimodal imaging agents offers the possibility of visual investigations of fibrillary tau pathologies at subcellular, cellular, and regional levels. These assay systems are potentially powerful tools for the longitudinal evaluation of anti-tau treatments (Marx, 2007), as a single probe may facilitate a seamless, bidirectional translation between preclinical and clinical insights. PET tracers would also serve a more immediate therapeutic purpose by enabling the assessment of the effects of anti-Aβ and anti-tau therapies on tau pathologies in living AD patients.

EXPERIMENTAL PROCEDURES

Compounds and Reagents

PBB1 (Wako Pure Chemical Industries), PBB2 (ABX), PBB3 (Nard Institute), PBB4 (ABX), mPBB5 (Nard Institute), desmethyl precursor of [^{11}C]PBB2 (2-[4-(4-aminophenyl)buta-1,3-dienyl]benzothiazol-6-ol; Nard Institute), desmethyl precursor of [^{11}C]PBB3 protected with a silyl group (5-[4-(6-tert-butyldimethylsilyloxy-benzothiazol-2-yl)buta-1,3-dienyl]pyridine-2-amine; Nard Institute), desmethyl precursor of [^{11}C]mPBB5 (2-[4-(4-dimethylaminophenyl) buta-1,3-dienyl]-3-ethyl-6-hydroxybenzothiazol-3-ium; Nard Institute), and 2-[8-(4-dimethylaminophenyl)octa-1,3,5,7-tetraenyl]-3-ethylbenzothiazol-3-ium (DM-POTEB; Nard Institute) were custom synthesized. Information on other chemicals is provided in the Supplemental Experimental Procedures. ClogP for each compound was calculated using ACD Chemsketch logP software (Advanced Chemistry Development).

Animal Models

Tg mice heterozygous for human T34 (4-repeat tau isoform with 1 N-terminal insert) with FTDP-17 P301S mutation driven by mouse prion protein promoter, also referred to as PS19 mice (Yoshiyama et al., 2007), were bred and kept on a C57BL/6 background. All mice studied here were maintained and handled in accordance with the National Research Council's Guide for the Care and Use of Laboratory Animals and our institutional guidelines. Protocols for the present animal experiments were approved by the Animal Ethics Committees of the National Institute of Radiological Sciences.

Postmortem Brain Tissues

Procedures for preparation of human and mouse brain sections are given in the Supplemental Experimental Procedures.

In Vitro and Ex Vivo Fluorescence Microscopy

Six micrometer paraffin sections generated from patient brains and 20 μm frozen sections of mouse brains were stained with 10^{-3}% β sheet ligands

dissolved in 50% ethanol for 1 hr at room temperature. Images of the fluorescence signals from these compounds were captured by nonlaser (BZ-9000; Keyence Japan) and confocal laser scanning (FV-1000; Olympus) microscopes. In the confocal imaging, excitation/emission wavelengths (nm) were optimized for each compound as follows: 405/420-520 (PBB3, FSB, PIB, BF-227, BF-158, FDDNP, thioflavin-S), 488/520-580 (PBB2, PBB4), 515/530-630 (PBB1, curcumin), and 635/645-720 (PBB5, BF-189, DM-POTEB). Subsequently, the tested samples and adjacent sections probed serially with each ligand were autoclaved for antigen retrieval, immunostained with the anti-tau monoclonal antibody AT8 that is specific for tau phosphorylated at Ser 202 and Thr 205 (Endogen), as well as a polyclonal antibody against AβN3(pE), and inspected using the microscopes noted above. For ex vivo imaging, PS19 and non-Tg WT at 10–12 months of age were anesthetized with 1.5% (v/v) isoflurane and were given 1 mg/kg PBB1-4, 0.1 mg/kg PBB5, or 10 mg/kg FSB by syringe via tail vein. The animals were killed by decapitation at 60 min after tracer administration. Brain and spinal cord were harvested and cut into 10-μm-thick sections on a cryostat (HM560). The sections were imaged using microscopes as in the in vitro assays and were labeled with either FSB or AT8, followed by microscopic re-examination.

Ex Vivo and In Vivo Multiphoton Imaging

Experimental procedures are given in the Supplemental Experimental Procedures.

In Vivo and Ex Vivo Pulsed Laser Scanning Imaging

Noninvasive scans of isoflurane-anesthetized non-Tg WT and tau Tg mice at 12 months of age were performed using a small animal-dedicated optical imager (eXplore Optix; ART). Scan protocols are given in the Supplemental Experimental Procedures.

Radiosynthesis of [^{11}C]PBB2

Experimental procedures are given in the Supplemental Experimental Procedures.

Radiosynthesis of [^{11}C]PBB3

[^{11}C]Methyl iodide was produced and transferred into 300 μl of dimethyl sulphoxide (DMSO) containing 1.5–2 mg of *tert*-butyldimethylsilyl desmethyl precursor and 10 mg of potassium hydroxide at room temperature. The reaction mixture was heated to 125°C and maintained for 5 min. After cooling the reaction vessel, 5 mg of *tetra-n*-butylammonium fluoride hydrate in 600 μl of water was added to the mixture to delete the protecting group, and then 500 μl of HPLC solvent was added to the reaction vessel. The radioactive mixture was transferred into a reservoir for HPLC purification (CAPCELL PAK C_{18} column, 10 × 250 mm; acetonitrile/50 mM ammonium formate = 4/6, 6 ml/min). The fraction corresponding to [^{11}C]PBB3 was collected in a flask containing 100 μl of 25% ascorbic acid solution and 75 μl of Tween 80 in 300 μl of ethanol and was evaporated to dryness under a vacuum. The residue was dissolved in 10 ml of saline (pH 7.4) to obtain [^{11}C]PBB3 (970–1,990 GBq at the end of synthesis [EOS]) as an injectable solution. The final formulated product was radiochemically pure (≥95%) as detected by analytic HPLC (CAPCELL PAK C_{18} column, 4.6 × 250 mm; acetonitrile/50 mM ammonium formate = 4/6, 2 ml/min). The specific activity of [^{11}C]PBB3 at EOS was 37–121 GBq/μmol, and [^{11}C]PBB3 maintained its radioactive purity exceeding 90% over 3 hr after formulation.

Radiosynthesis of [^{11}C]mPBB5

Experimental procedures are given as Supplemental Experimental Procedures.

Radiosynthesis of [^{11}C]PIB

Radiolabeling of PIB was performed as described elsewhere (Maeda et al., 2011). The specific activity of [^{11}C]PIB at EOS was 50–110 GBq/μmol.

In Vitro and Ex Vivo Autoradiography

Experimental procedures are given in the Supplemental Experimental Procedures.

In Vivo PET Imaging of Mice

PET scans were performed using a microPET Focus 220 animal scanner (Siemens Medical Solutions) immediately after intravenous injection of [^{11}C]PBB2 (28.3 ± 10.3 MBq), [^{11}C]PBB3 (29.7 ± 9.3 MBq), or [^{11}C]mPBB5 (32.8 ± 5.9 MBq). Detailed procedures are provided in the Supplemental Experimental Procedures.

In Vivo PET Imaging of Humans

Three cognitively normal control subjects (64, 72, and 75 years of age; mean age, 70.3 years) and three AD patients (64, 75 and 77 years of age; mean age, 72 years) were recruited to the present work (Figure 8). Additional information on these subjects is given in the Supplemental Experimental Procedures. The current clinical study was approved by the Ethics and Radiation Safety Committees of the National Institute of Radiological Sciences. Written informed consent was obtained from the subjects or their family members. PET assays were conducted with a Siemens ECAT EXACT HR+ scanner (CTI PET Systems). Detailed PET scan protocols are provided in the Supplemental Experimental Procedures. A fraction of radioactivity corresponding to unmetabolized [^{11}C]PBB3 in plasma at 3, 10, 20, 30, and 60 min was determined by HPLC (Waters mBondapak C_{18} column, 7.8 × 300 mm; acetonitrile/ammonium formate mobile phase with gradient elution = 40/60, 52/48, 80/20, 80/20, 40/60, and 40/60 at 0, 6, 7, 8, 9, and 15 min, respectively; flow rate, 6 ml/min) as described elsewhere (Suzuki et al., 1999). The radiotracer injection and following scans and plasma assays were conducted in a dimly lit condition to avoid photoracemization of the chemicals.

Individual MRI data were coregistered to the PET images using PMOD software (PMOD Technologies). Volumes of interest (VOIs) were drawn on coregistered MR images and were transferred to the PET images. Procedures of image analyses are provided in the Supplemental Experimental Procedures.

We additionally carried out PET scans of a patient who was clinically diagnosed as having corticobasal syndrome, as described in the Supplemental Experimental Procedures.

SUPPLEMENTAL INFORMATION

Supplemental Information includes Supplemental Experimental Procedures, nine figures, and one table and can be found with this article online at http://dx.doi.org/10.1016/j.neuron.2013.07.037.

ACKNOWLEDGMENTS

The authors thank Mr. T. Minamihisamatsu and Mr. Y. Matsuba for technical assistance, the staff of the Molecular Probe Group, National Institute of Radiological Sciences, for support with radiosynthesis, Dr. Y. Yoshiyama at National Hospital Organization Chiba-East Hospital for his support on clinical PET studies, and Dr. T. Iwatsubo at the University of Tokyo and Dr. H. Inoue at Kyoto University for their critical discussions. This work was supported in part by grants from the National Institute on Aging of the National Institutes of Health (AG10124 and AG17586) (to J.Q.T. and V. M.-Y.L.), Grants-in-Aid for Japan Advanced Molecular Imaging Program, Young Scientists (21791158) (to M.M.), Scientific Research (B) (23390235) (to M.H.), Core Research for Evolutional Science and Technology (to T.S.), Scientific Research on Innovative Areas ("Brain Environment") (23111009) (to M.H.) from the Ministry of Education, Culture, Sports, Science and Technology, Japan, Thomas H. Maren Junior Investigator Fund from College of Medicine, University of Florida (to N.S.), and research fund of Belfer Neurodegeneration Consortium (to Q.C. and M.-K.J.). M.M., H. Shimada, T.S., M.-R.Z., and M.H. are named as inventors on a patent application 0749006WO1, claiming subject matter related to the results described in this paper.

Accepted: July 12, 2013
Published: September 18, 2013

REFERENCES

Bacskai, B.J., Hickey, G.A., Skoch, J., Kajdasz, S.T., Wang, Y., Huang, G.F., Mathis, C.A., Klunk, W.E., and Hyman, B.T. (2003). Four-dimensional

multiphoton imaging of brain entry, amyloid binding, and clearance of an amyloid-β ligand in transgenic mice. Proc. Natl. Acad. Sci. USA *100*, 12462–12467.

Ballatore, C., Lee, V.M.Y., and Trojanowski, J.Q. (2007). Tau-mediated neurodegeneration in Alzheimer's disease and related disorders. Nat. Rev. Neurosci. *8*, 663–672.

Braak, H., and Braak, E. (1991). Neuropathological stageing of Alzheimer-related changes. Acta Neuropathol. *82*, 239–259.

Braak, H., Thal, D.R., Ghebremedhin, E., and Del Tredici, K. (2011). Stages of the pathologic process in Alzheimer disease: age categories from 1 to 100 years. J. Neuropathol. Exp. Neurol. *70*, 960–969.

Chien, D.T., Bahri, S., Szardenings, A.K., Walsh, J.C., Mu, F., Su, M.Y., Shankle, W.R., Elizarov, A., and Kolb, H.C. (2013). Early clinical PET imaging results with the novel PHF-tau radioligand [F-18]-T807. J. Alzheimers Dis. *34*, 457–468.

Dickson, D.W., Kouri, N., Murray, M.E., and Josephs, K.A. (2011). Neuropathology of frontotemporal lobar degeneration-tau (FTLD-tau). J. Mol. Neurosci. *45*, 384–389.

Engler, H., Forsberg, A., Almkvist, O., Blomquist, G., Larsson, E., Savitcheva, I., Wall, A., Ringheim, A., Långström, B., and Nordberg, A. (2006). Two-year follow-up of amyloid deposition in patients with Alzheimer's disease. Brain *129*, 2856–2866.

Fodero-Tavoletti, M.T., Okamura, N., Furumoto, S., Mulligan, R.S., Connor, A.R., McLean, C.A., Cao, D., Rigopoulos, A., Cartwright, G.A., O'Keefe, G., et al. (2011). ^{18}F-THK523: a novel *in vivo* tau imaging ligand for Alzheimer's disease. Brain *134*, 1089–1100.

Higuchi, M., Iwata, N., Matsuba, Y., Sato, K., Sasamoto, K., and Saido, T.C. (2005). ^{19}F and ^{1}H MRI detection of amyloid β plaques *in vivo*. Nat. Neurosci. *8*, 527–533.

Hintersteiner, M., Enz, A., Frey, P., Jaton, A.L., Kinzy, W., Kneuer, R., Neumann, U., Rudin, M., Staufenbiel, M., Stoeckli, M., et al. (2005). *In vivo* detection of amyloid-β deposits by near-infrared imaging using an oxazine-derivative probe. Nat. Biotechnol. *23*, 577–583.

Klunk, W.E., Wang, Y., Huang, G.F., Debnath, M.L., Holt, D.P., Shao, L., Hamilton, R.L., Ikonomovic, M.D., DeKosky, S.T., and Mathis, C.A. (2003). The binding of 2-(4′-methylaminophenyl)benzothiazole to postmortem brain homogenates is dominated by the amyloid component. J. Neurosci. *23*, 2086–2092.

Klunk, W.E., Engler, H., Nordberg, A., Wang, Y., Blomqvist, G., Holt, D.P., Bergström, M., Savitcheva, I., Huang, G.F., Estrada, S., et al. (2004). Imaging brain amyloid in Alzheimer's disease with Pittsburgh Compound-B. Ann. Neurol. *55*, 306–319.

Krebs, M.R.H., Bromley, E.H., and Donald, A.M. (2005). The binding of thioflavin-T to amyloid fibrils: localisation and implications. J. Struct. Biol. *149*, 30–37.

Kudo, Y., Okamura, N., Furumoto, S., Tashiro, M., Furukawa, K., Maruyama, M., Itoh, M., Iwata, R., Yanai, K., and Arai, H. (2007). 2-(2-[2-Dimethylaminothiazol-5-yl]ethenyl)-6- (2-[fluoro]ethoxy)benzoxazole: a novel PET agent for *in vivo* detection of dense amyloid plaques in Alzheimer's disease patients. J. Nucl. Med. *48*, 553–561.

Maeda, J., Ji, B., Irie, T., Tomiyama, T., Maruyama, M., Okauchi, T., Staufenbiel, M., Iwata, N., Ono, M., Saido, T.C., et al. (2007). Longitudinal, quantitative assessment of amyloid, neuroinflammation, and anti-amyloid treatment in a living mouse model of Alzheimer's disease enabled by positron emission tomography. J. Neurosci. *27*, 10957–10968.

Maeda, J., Zhang, M.R., Okauchi, T., Ji, B., Ono, M., Hattori, S., Kumata, K., Iwata, N., Saido, T.C., Trojanowski, J.Q., et al. (2011). *In vivo* positron emission tomographic imaging of glial responses to amyloid-beta and tau pathologies in mouse models of Alzheimer's disease and related disorders. J. Neurosci. *31*, 4720–4730.

Marx, J. (2007). Alzheimer's disease. A new take on tau. Science *316*, 1416–1417.

Okamura, N., Suemoto, T., Furumoto, S., Suzuki, M., Shimadzu, H., Akatsu, H., Yamamoto, T., Fujiwara, H., Nemoto, M., Maruyama, M., et al. (2005). Quinoline and benzimidazole derivatives: candidate probes for *in vivo* imaging of tau pathology in Alzheimer's disease. J. Neurosci. *25*, 10857–10862.

Santacruz, K., Lewis, J., Spires, T., Paulson, J., Kotilinek, L., Ingelsson, M., Guimaraes, A., DeTure, M., Ramsden, M., McGowan, E., et al. (2005). Tau suppression in a neurodegenerative mouse model improves memory function. Science *309*, 476–481.

Schmidt, M.L., Gur, R.E., Gur, R.C., and Trojanowski, J.Q. (1988). Intraneuronal and extracellular neurofibrillary tangles exhibit mutually exclusive cytoskeletal antigens. Ann. Neurol. *23*, 184–189.

Small, G.W., Kepe, V., Ercoli, L.M., Siddarth, P., Bookheimer, S.Y., Miller, K.J., Lavretsky, H., Burggren, A.C., Cole, G.M., Vinters, H.V., et al. (2006). PET of brain amyloid and tau in mild cognitive impairment. N. Engl. J. Med. *355*, 2652–2663.

Suzuki, K., Takei, M., and Kida, T. (1999). Development of an analyzing system for the sensitive measurement of radioactive metabolites on the PET study. J. Labelled Comp. Radiopharm. *42*, S658–S660.

Thompson, P.W., Ye, L., Morgenstern, J.L., Sue, L., Beach, T.G., Judd, D.J., Shipley, N.J., Libri, V., and Lockhart, A. (2009). Interaction of the amyloid imaging tracer FDDNP with hallmark Alzheimer's disease pathologies. J. Neurochem. *109*, 623–630.

Yang, L., Rieves, D., and Ganley, C. (2012). Brain amyloid imaging—FDA approval of florbetapir F18 injection. N. Engl. J. Med. *367*, 885–887.

Yoshiyama, Y., Higuchi, M., Zhang, B., Huang, S.M., Iwata, N., Saido, T.C., Maeda, J., Suhara, T., Trojanowski, J.Q., and Lee, V.M.Y. (2007). Synapse loss and microglial activation precede tangles in a P301S tauopathy mouse model. Neuron *53*, 337–351.

Zhang, W., Arteaga, J., Cashion, D.K., Chen, G., Gangadharmath, U., Gomez, L.F., Kasi, D., Lam, C., Liang, Q., Liu, C., et al. (2012). A highly selective and specific PET tracer for imaging of tau pathologies. J. Alzheimers Dis. *31*, 601–612.

Zhuang, Z.P., Kung, M.P., Hou, C., Skovronsky, D.M., Gur, T.L., Plössl, K., Trojanowski, J.Q., Lee, V.M.Y., and Kung, H.F. (2001). Radioiodinated styrylbenzenes and thioflavins as probes for amyloid aggregates. J. Med. Chem. *44*, 1905–1914.

MOLECULAR IMAGING AND BIOLOGY

Mol Imaging Biol (2013)
DOI: 10.1007/s11307-013-0667-2

World Molecular Imaging Society

RESEARCH ARTICLE

Use of a Benzimidazole Derivative BF-188 in Fluorescence Multispectral Imaging for Selective Visualization of Tau Protein Fibrils in the Alzheimer's Disease Brain

Ryuichi Harada,[1] Nobuyuki Okamura,[1] Shozo Furumoto,[1] Takeo Yoshikawa,[1] Hiroyuki Arai,[2] Kazuhiko Yanai,[1] Yukitsuka Kudo[3]

[1]*Department of Pharmacology, Tohoku University School of Medicine, 2-1, Seiryo-machi, Aoba-ku, Sendai, 980-8575, Japan*
[2]*Department of Geriatrics and Gerontology, Institute of Development, Aging and Cancer, Tohoku University, Sendai, Japan*
[3]*Clinical Research, Innovation and Education Center, Tohoku University Hospital, Sendai, Japan*

Abstract

Purpose: Selective visualization of amyloid-β and tau protein deposits will help to understand the pathophysiology of Alzheimer's disease (AD). Here, we introduce a novel fluorescent probe that can distinguish between these two deposits by multispectral fluorescence imaging technique.

Procedures: Fluorescence spectral analysis was performed using AD brain sections stained with novel fluorescence compounds. Competitive binding assay using [^{3}H]-PiB was performed to evaluate the binding affinity of BF-188 for synthetic amyloid-β (Aβ) and tau fibrils.

Results: In AD brain sections, BF-188 clearly stained Aβ and tau protein deposits with different fluorescence spectra. *In vitro* binding assays indicated that BF-188 bound to both amyloid-β and tau fibrils with high affinity (K_i<10 nM). In addition, BF-188 showed an excellent blood–brain barrier permeability in mice.

Conclusion: Multispectral imaging with BF-188 could potentially be used for selective *in vivo* imaging of tau deposits as well as amyloid-β in the brain.

Key words: Multispectral fluorescence imaging, Fluorescent probes, Neurofibrillary tangles, Senile plaques, Alzheimer's disease

Introduction

Alzheimer's disease (AD) is pathologically characterized by the deposition of senile plaques (SPs) and neurofibrillary tangles (NFTs). SPs are composed of amyloid-β (Aβ) peptide that is derived from amyloid precursor protein. NFTs comprise bundles of paired helical filaments (PHFs) that result from the abnormal aggregation of hyperphosphorylated tau protein. According to the amyloid cascade hypothesis, Aβ accumulation leads to its aggregation and formation of SPs, followed by formation of NFTs, synaptic dysfunction, and neuronal death. However, Aβ and tau are thought to act synergistically to promote the accumulation of each protein and to accelerate development of cognitive dysfunction [1]. To precisely monitor the progression of AD-related pathology, it is desirable to visualize both Aβ and tau protein deposits separately.

Recently, multispectral fluorescence imaging (MSFI) has been widely used for preclinical applications in microscopy

Electronic supplementary material The online version of this article (doi:10.1007/s11307-013-0667-2) contains supplementary material, which is available to authorized users.

Correspondence to: Nobuyuki Okamura; *e-mail:* nookamura@med.tohoku.ac.jp

Published online: 19 July 2013

and small-animal imaging. This technique can distinguish crude fluorescence signals from multiple fluorophores into individual contributors based on their fluorescence spectra [2]. MSFI can be used to improve signal-to-background ratio by separating the signals of the bound probe from those of the unbound probe and autofluorescence [3]. Another application of MSFI is identification of different protein aggregates, because some fluorescence compounds show different Stoke's shift of the wavelength to various protein fibrils [4]. We previously found that a benzimidazole derivative, BF-126, emitted a different color of fluorescence when it was bound to Aβ and tau [5]. This finding suggested that these two protein deposits can be differentiated by MSFI technique using a single fluorescence probe.

To identify wavelength-responsive β-sheet binding probes, we screened our compound library and discovered a novel fluorescent probe, 2-[[4-(4-methylamino)phenyl]-1,3-butadienyl]benzimidazole (BF-188) that showed a prominent redshift only on binding to tau protein aggregates in AD brain. Here, we show the wavelength-dependent identification of tau protein deposits by MSFI using BF-188.

Methods

Materials

Six fluorescence compounds, (4-[2-(2-benzothiazolyl)ethenyl]-*N,N*-diethylbenzenamine (BF-124), 4-[2-(2-benzoxazolyl)ethenyl]-*N,N*-diethylbenzenamine (BF-125), 4-[2-(2-benzoimidazolyl)ethenyl]-*N,N*-diethylbenzenamine (BF-126), 2-[[4-(4-methylamino)phenyl]-1,3-butadienyl]benzoxazole (BF-185), 2-[[4-(4-methylamino)phenyl]-1,3-butadienyl]benzothiazole (BF-187), 2-[[4-(4-methylamino)phenyl]-1,3-butadienyl]benzimidazole (BF-188)), were originally designed by us and custom-synthesized by Tanabe R&D Service (Osaka, Japan). Chemical structures of these compounds are shown in Fig. 2. As these compounds have some methine chains in their structure, they can form *E/Z* isomers. However, we confirmed that these compounds exist as an *E* isomer in the solution (Fig. S1). 1,4-Bis[2-(3-carboxy-4-hydroxyphenyl)ethenyl]-benzene disodium salt (X-34) [6], 2-(1-{6-[(2-fluoroethyl)-methylamino]-2-naphthyl}ethylidene)malononitrile (FDDNP), and 2-[4-(methylamino)phenyl]-6-hydroxybenzothiazole (PiB) were also synthesized by Tanabe R&D Service. 1-Fluoro-2,5-bis(3-carboxy-4-hydroxystyryl)benzene (FSB) [7] was purchased from Dojindo (Tokyo, Japan). Thioflavin-S was obtained from Sigma (Saint Louis, Mo). Nile red was purchased from Organica (Wolfen, Germany). [^{3}H]PiB (specific activity, 2,960 GBq/mmol) was purchased from American Radiolabeled Chemicals (Saint Louis, Mo). Human $A\beta_{42}$ was purchased from Peptide Institute Inc. (Mino, Japan). Recombinant K18ΔK280-tau protein was obtained from Life Technologies (Tokyo, Japan).

Neuropathological Staining and Spectral Analysis

Experiments were performed under the regulations of the ethics committee of Tohoku University School of Medicine. Postmortem brain tissues from four autopsy-confirmed AD cases (90-, 82-, and 68-year-old females and 85-year-old male) and one dementia with Lewy bodies (DLB) case (64-year-old female) were obtained from Fukushimura Hospital (Toyohashi, Japan). Serial sections (6 μm thickness) from paraffin-embedded blocks of the frontal and temporal cortices and hippocampus were prepared in xylene and ethanol. Test compounds (100 μM) were dissolved in 50 % ethanol solution. Tissue sections were then immersed in 100 μM test compounds or 0.125 % thioflavin-S solution for 10 min. Finally, the sections were dipped briefly into water, washed in 50 % ethanol, rinsed in phosphate buffer, and examined using a fluorescence microscope (Eclipse 80i; Nikon, Tokyo, Japan) equipped with an ultraviolet filter (excitation, 365/10 nm; dichroic mirror, 400 nm; barrier filter, 400 nm), a violet filter (excitation, 380–420 nm; dichroic mirror, 430 nm; barrier filter, 450 nm), a blue–violet filter (excitation, 400–440 nm; dichroic mirror, 455 nm; barrier filter, 470 nm), and a blue filter (excitation, 450–490 nm; dichroic mirror, 505 nm; barrier filter, 520 nm). Fluorescence spectra were recorded with a multispectral imaging system (Nuance FX, Caliper, Hopkinton, MA) and analyzed with the Nuance software. In the analysis of fluorescence spectra, the background fluorescence spectra were subtracted from the whole fluorescence spectra, to identify the fluorescence signals derived from specific binding. Then, the fluorescence intensity at each wavelength was normalized by the maximum fluorescence intensity at the peak wavelength.

Fluorescence and Immunohistochemical Analysis

Immunostaining was performed using monoclonal antibodies against Aβ (6F/3D; Dako, Glostrup, Denmark) at a dilution of 1:50, phosphorylated tau (AT8; Innnogenetics, Ghent, Belgium) at a dilution of 1:20, dephosphorylated tau (Tau-1; Millipore, Billerica, MA) at a dilution of 1:200, and phosphorylated α-synuclein (pSyn#64; Wako Pure Chemicals, Tokyo, Japan) at a dilution of 1:2,000. For tau and α-synuclein immunostaining, antigen unmasking was performed using UNI-TRIEVE solution (Innnogenetics) after deparaffinization. For Aβ immunostaining, sections were treated with 90 % formic acid for 5 min. These sections were placed in blocking buffer for 30 min and then incubated at 4 °C with primary antibody for 18 h. After washing, the sections were incubated first with biotinylated anti-mouse IgG (Wako Pure Chemicals) for 60 min, and then with Alexa Fluor® 350-conjugated streptavidin (Life Technologies) for tau immunostaining and Texas Red-conjugated streptavidin (Vector Laboratories, Burlingame, CA) for Aβ and α-synuclein immunostaining. Immunostained sections were immersed in 1 μM of each compound and then examined using a Nikon Eclipse microscope. An adjacent section was used for Aβ immunostaining. For dephosphorylation of tau, the sections were treated with 16.7 units of *Escherichia coli* alkaline phosphatase (Sigma) at 67 °C for 3 h [8]. After washing, tau immunostaining was conducted according to the above protocol.

In Vitro Competitive Binding of Amyloid and Tau Fibrils

Synthetic $A\beta_{42}$ and tau fibrils were prepared as previously described [9]. We used truncated tau construct (K18ΔK280) fibrils for the *in vitro* binding study, because this construct shows similar characteristics to PHF-tau from AD brain and forms aggregates quickly without any co-factor. For the *in vitro* competitive binding

assays, synthetic $A\beta_{42}$ or K18ΔK280 fibrils (200 nM) were incubated with increasing concentrations (0.1–1,000 nM) of unlabeled PiB and BF-188 in the presence of 1 nM of [^{3}H]PiB for 3 h at room temperature. Separation of bound and free radioactivity was achieved by filtration under reduced pressure (MultiScreen HTS Vacuum Manifold; MultiScreen HTS 96-well 0.65 μm filtration plate, Millipore). Filters were washed with 200 μl assay buffer (Dulbecco's phosphate-buffered saline; 0.1 % bovine serum albumin) thrice, and filters containing [^{3}H]PiB were incubated in 2 ml of scintillation fluid (Aquasol-2, PerkinElmer, Boston, MA). Radioactivity of ^{3}H was counted in a beta counter (LS6500 liquid scintillation counter; Beckman Coulter, Brea, CA). Binding data were analyzed with curve fitting software that calculates the K_i using a one-site competition model (GraphPad Prism Version 5.0, GraphPad Software, San Diego, CA).

Brain Uptake of BF-188 and PiB in Normal Mice

The experimental protocol of animal study was approved by the Ethics Committee of Tohoku University School of Medicine. Brain uptake after intravenous injection of the compounds in mice was analyzed using high-performance liquid chromatography with a fluorescence detector, as described previously [5]. The test compounds can be dissolved in saline containing 5 % EtOH and 5 % Tween 80. Briefly, each compound (1 mg/kg) was administered into the tail vein of male Institute of Cancer Research (ICR) mice (7 weeks of age; body weight, 30–40 g; n=3). At 2 and 30 min after the injection of the compounds, the brain was removed. Brain samples were homogenized and centrifuged at 14,000 rpm for 10 min, and the supernatant was used for extraction. The mobile phase was 20 mM phosphate buffer, pH 6.5, and acetonitrile at a ratio 3:7 for BF-188, 11:9 for PiB at a flow rate of 1 ml/min. For preparing standards, the compounds were mixed with brain homogenate. To measure the compound's fluorescence, FS-8020 fluorescence detector (Tosoh, Tokyo, Japan) was operated at excitation/emission wavelengths of 350/420 nm for PiB and 390/525 nm for BF-188. The amounts of test compounds in the brain were calculated from the peak areas at the retention time of the standard samples. Finally, the percentage of injected dose per gram (%ID/g) was determined using weights of brain samples.

Results

Fluorescence Spectra of Test Compounds for SPs and NFTs

Firstly, we performed spectral analysis of AD frontal brain sections stained with several β-sheet binding compounds, to check whether the compounds show the difference in fluorescence spectra for SPs and NFTs (Table 1). All test compounds clearly stained both SPs and NFTs in AD brain sections (Fig. 1). As expected, BF-126 exhibited different fluorescence spectra when it was bound to SPs and NFTs in AD brain sections. Maximal emission wavelength of BF-126 was 490 nm for SPs and 540 nm for NFTs (Fig. 2a). In contrast, a benzothiazole derivative, BF-124, and a benzoxazole derivative, BF-125, showed no remarkable difference in the fluorescence spectra after binding to SPs and NFTs (Fig. 2b, c). Furthermore, the other BF compounds showed the same tendency of fluorescence property except to BF-188 (Fig. 2e–g). Only the benzimidazole derivative BF-188 showed a difference in the fluorescence spectra when it was bound to SPs and NFTs in AD brain tissue (Fig. 2e). These findings indicate that the benzimidazole framework is necessary for the expression of redshift on tau protein fibrils. The maximum peaks of BF-188 fluorescence spectra were 520 nm for SPs and 600 nm for NFTs, indicating a greater redshift than that for BF-126 (Fig. 2e). We observed consistent results from different brain regions (the temporal cortex and hippocampus) and different AD patients' samples (Fig. 3). However, we did not observe a difference in the fluorescence spectra of BF-188 on binding to synthetic Aβ and tau fibrils, suggesting that the structural conformation of synthetic protein fibrils is different from native protein deposits in the human brain. Thioflavin-S (Fig. 2k), X-34 (Fig. 2d), and FSB (Fig. 2h) did not show a difference in the fluorescence spectra on binding to SPs and NFTs. A previous study showed a difference in the fluorescence spectra of Nile red bound to various amyloid fibrils (Fig. 2j) [4]. Our study indicated that the difference in Nile red fluorescence spectra on binding to SPs and NFTs was smaller than that in BF-188 fluorescence spectra (Table 1). We performed MSFI to visualize BF-188 staining in the AD brain section and were able to clearly distinguish between SPs and NFTs (Fig. 4a–e). The binding of BF-188 to PHF-tau was confirmed by tau immunostaining in the same section (Fig. 4f). Likewise, the binding of BF-188 to SPs was confirmed by Aβ immunostaining in the adjacent section (Fig. 4g).

Wavelength-Dependency of BF-188 Fluorescence in Senile Plaques, Neurofibrillary Tangles, and Lewy Bodies in Human Brain Tissues

We further investigated the wavelength-dependency of BF-188 fluorescence in AD brain sections using conventional fluorescence microscopy equipped with various filters. Even without using MSFI, the fluorescence signals from SPs and NFTs are clearly separated by BF-188 staining. BF-188 clearly stained both SPs and NFTs under a blue-violet excitation filter (λ_{ex}=400–440 nm), whereas SPs and NFTs could be selectively visualized under violet and green filters, respectively (Fig. 4g–k). In brain sections from a case of DLB, we observed BF-188 binding to Lewy bodies (LBs) (Fig. 4l–m). The fluorescence spectrum of BF-188 on LBs was almost the same as that on SPs but different from that on NFTs (Fig. 4n).

The Effect of Phosphorylation of Tau Deposits on Fluorescence Property BF-188

We investigated the effect of tau phosphorylation on the BF-188 fluorescence property, because NFTs in AD brain are composed of hyperphosphorylated tau protein. Even after dephosphorylation by alkaline phosphatase, NFTs were

Table 1. Fluorescence profiles of test compounds on binding to senile plaques and neurofibrillary tangles

Compound	Maximal emission wavelength (nm)		Difference (nm)
	SPs	NFTs	
BF-124	510	530	20
BF-125	510	510	0
BF-126	490	540	50
BF-185	540	540	0
BF-187	540	540	0
BF-188	520	600	80
Thioflavin-S	510	520	10
X-34	550	550	0
FSB	530	530	0
Nile red	630	640	10
FDDNP	550	580	30

SPs senile plaques, *NFTs* neurofibrillary tangles

positively stained with both BF-188 and the Tau-1 antibody that recognizes unphosphorylated tau but not with the AT8 antibody that is specific for hyperphosphorylated tau (Fig. 5). This finding indicates that the BF-188 fluorescence property is independent of tau phosphorylation. Since imidazole derivatives are well-known pH indicators [10], we further investigated the effect of acidity on their fluorescence staining. However, we did not find any difference in BF-188 staining in the acidic condition (pH~6) and neutral condition (pH 7.3) (data not shown).

Binding Affinity of BF-188 to Synthetic $A\beta_{42}$ and Tau Fibrils

To evaluate the binding affinity of BF-188 for synthetic $A\beta_{42}$ and tau construct (K18ΔK280) fibrils, we conducted an *in vitro* competitive binding assay using ^{3}H-labeled PiB. BF-188 displaced [^{3}H]PiB bound to synthetic $A\beta_{42}$ and tau fibrils. $A\beta_{42}$ fibril binding affinity of BF-188 (K_i=6.3 nM) was comparable to that of PiB (K_i=5.7 nM). Furthermore, compared with PiB (K_i=8.2 nM), BF-188 showed higher binding affinity (K_i=3.9 nM) for tau fibrils.

Blood–Brain Barrier Permeability of BF-188 in Normal Mice

We investigated the blood–brain barrier permeability of BF-188 in normal (ICR) mice. Brain uptake 2 min after intravenous injection of BF-188 was 4.8%ID/g. In addition, BF-188 was rapidly washed out (0.12%ID/g) from the normal brain 30 min after injection (Supplementary Material, Fig. S2), indicating

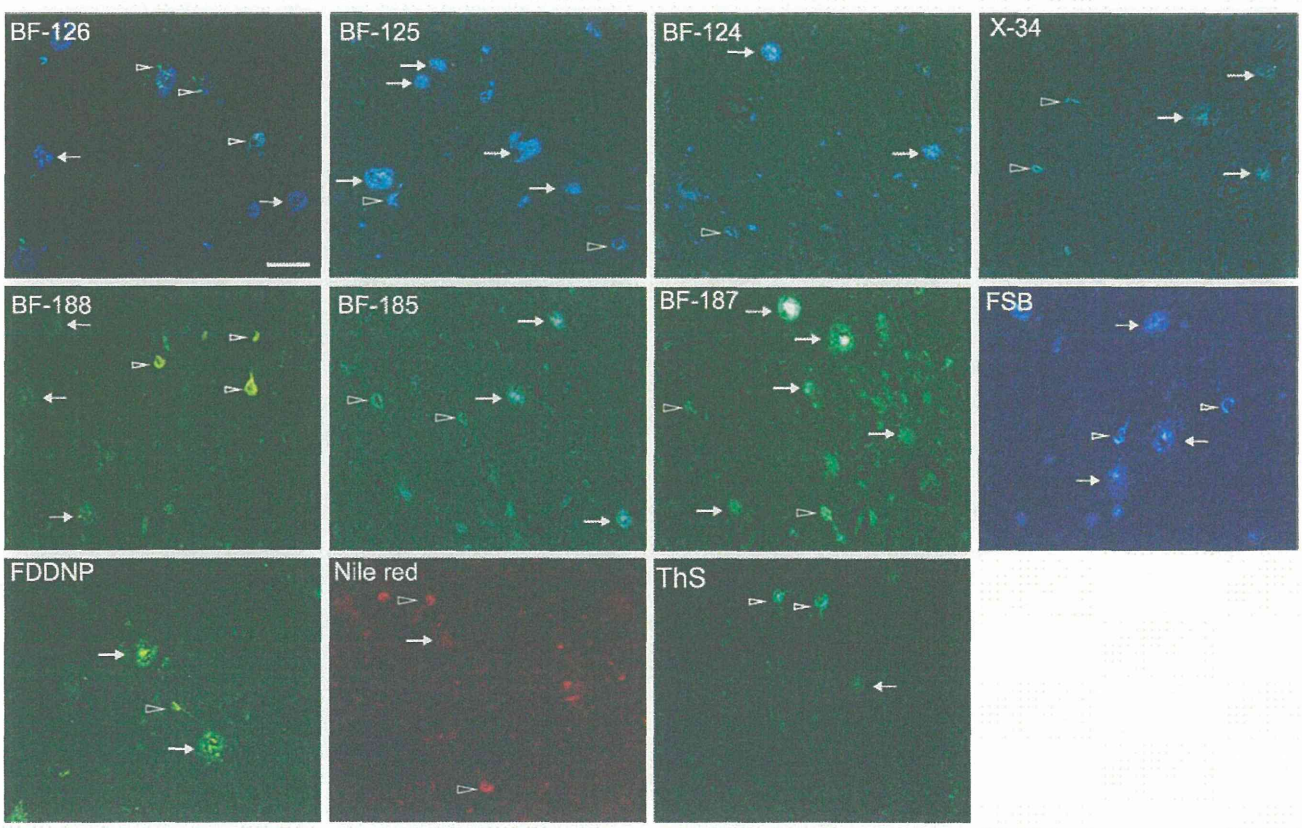

Fig. 1. Fluorescence microscopic images of BF-124, BF-125, BF-126, BF-185, BF-187, BF-188, X-34, FDDNP, Nile red, and thioflavin-S (ThS) bound to senile plaques (*arrows*) and neurofibrillary tangles (*arrowheads*) in AD frontal brain tissue. Scale *bars*, 50 μm.

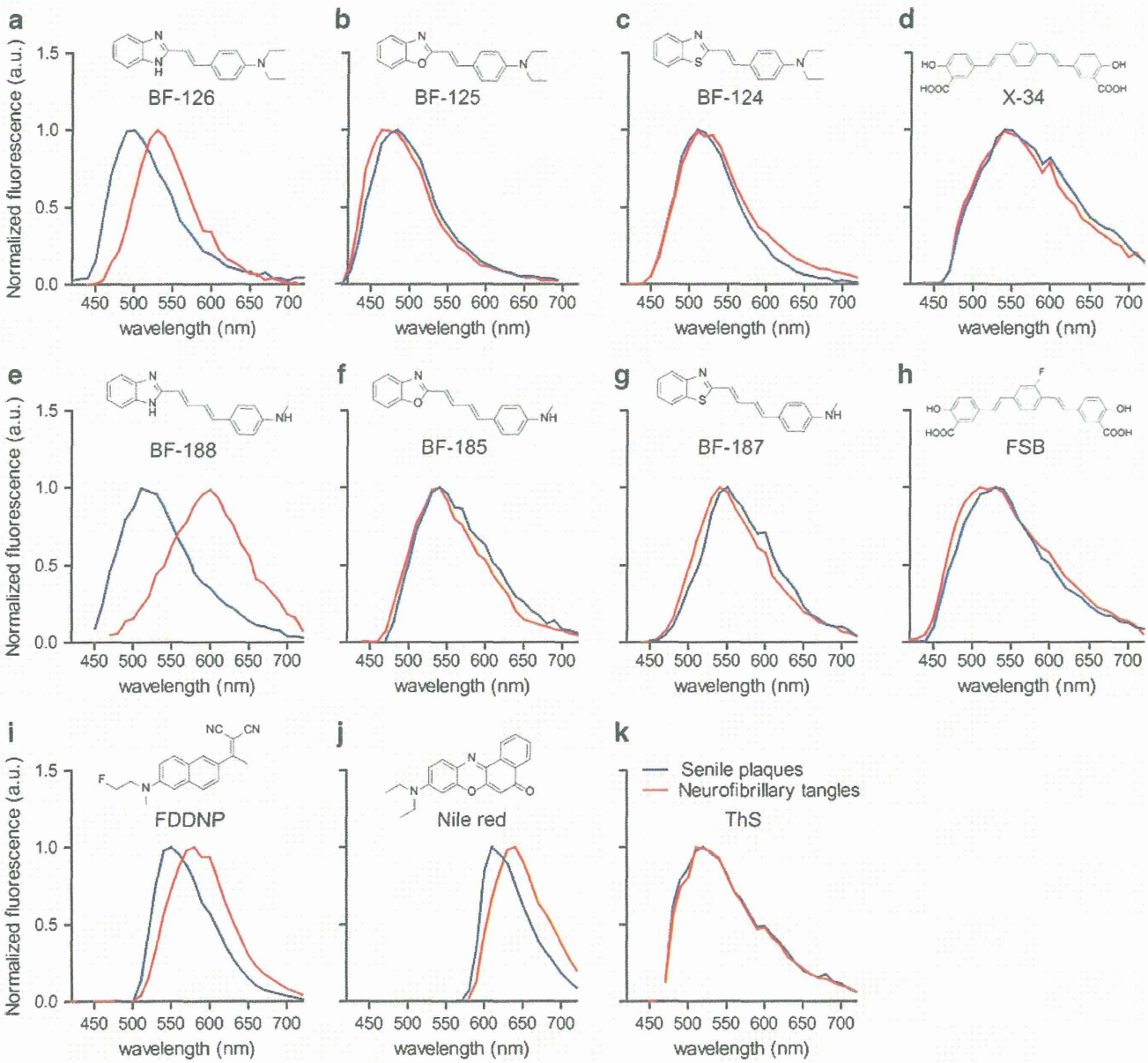

Fig. 2. Fluorescence spectra and chemical structures of BF-126 (**a**), BF-125 (**b**), BF-124 (**c**), X-34 (**d**), BF-188 (**e**), BF-185 (**f**), BF-187 (**g**), FSB (**h**), FDDNP (**i**), Nile red (**j**), and Thioflavin-S (**k**) bound to senile plaques (*arrows*) and neurofibrillary tangles (*arrowheads*) in Alzheimer's disease frontal brain sections. All spectra were recorded with a multispectral imaging system (Nuance FX, Caliper).

that this probe can potentially be used for *in vivo* brain imaging following intravenous administration.

Discussion

MSFI has been receiving attention as a technology to detect multiple fluorescence signals separately, thus providing a way to simultaneously monitor different pathophysiological information. In addition, MSFI can enhance the sensitivity to detect specific fluorescence signals in the human brain, by eliminating non-specific and autofluorescence signals from the background. To identify multiple targets simultaneously, MSFI generally requires more than one probe [11]. However, BF-188 allowed us to differentiate two histopathological hallmarks of AD (SPs and NFTs) without using multiple probes. SPs and NFTs share a common cross β-structure in which individual β-strands run perpendicular to the fiber axis [12]. In general, many amyloid binding reagents such as ThS and Congo Red interact with both Aβ and tau deposits such that their long axes align in a parallel fashion. These amyloid-binding dyes stain and emit the same fluorescence wavelength after binding to both SPs and NFTs. However, we observed that benzimidazole

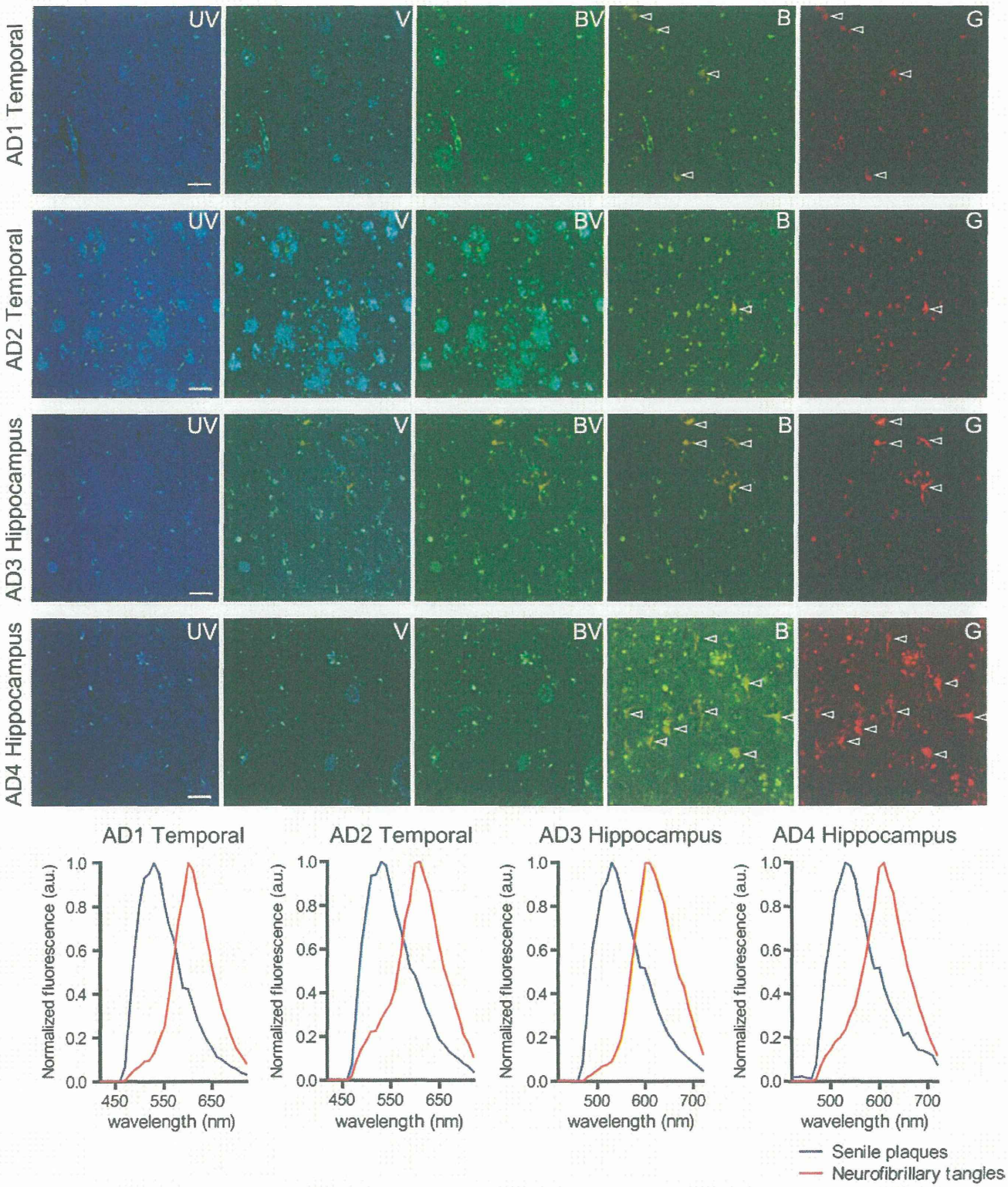

Fig. 3. Fluorescence microscopic images of BF-188 bound to senile plaques and neurofibrillary tangles (*arrowheads*) in various brain regions (temporal cortex and hippocampus) and different AD patients' samples. The fluorescence images were recorded when excited at an ultraviolet (*UV*) filter, a violet (*V*) filter, a blue–violet (*BV*) filter, a blue (*B*) filter, and a green (*G*) filter, respectively. Fluorescence spectra of BF-188 were shown in the below images. Scale *bars*, 50 μm.